Available online at www.sciencedirect.com
SCIENCE DIRECT®
Journal of Solid State Chemistry 170 (2003) 94–105
JOURNAL OF SOLID STATE CHEMISTRY
http://elsevier.com/locate/jssc

# $Ba_{14}Zn_{5-x}Al_{22+x}$: a new polar intermetallic compound with a novel 2D network

Chi-Shen Lee and Gordon J. Miller*

*Department of Chemistry, Iowa State University, Ames, IA 50011-3111, USA*

Received 30 April 2002; received in revised form 5 August 2002; accepted 27 August 2002

**Abstract**

A new ternary, intermetallic compound, $Ba_{14}Zn_{5-x}Al_{22+x}$, was synthesized by heating the pure elements at 900°C. This compound crystallizes in the monoclinic space group $I2/m$, $Z=2$, with $a=10.474(2)$ Å, $b=6.0834(14)$ Å, $c=34.697(8)$ Å and $\beta=90.814(4)^\circ$. The crystal structure of $Ba_{14}Zn_{5-x}Al_{22+x}$ consists of $[Zn_{5-x}Al_{22+x}]$ slabs that are built with a novel, two-dimensional (2D) network of Zn and Al atoms involving eight-membered rings sandwiched between two layers of trigonal bipyramids interconnected by three-center bonding. Tight-binding, linear muffin–tin orbital (TB-LMTO-ASA) calculations have been performed to understand the relationship between composition and orbital interactions in the electronegative element framework. This new structure is closely related to the high-pressure, cubic Laves-type structure of $BaAl_2$ as well as the ambient pressure binary compound, $Ba_7Al_{13}$. The degree of valence electron charge transfer from the electropositive Ba atoms is related to the Al:Ba molar ratio in the Ba–Zn–Al system.


*Keywords:* Intermetallics; Crystal structure; Electronic structure

## 1. Introduction

Intermetallic compounds offer numerous opportunities to examine the relationships among composition, structure and chemical bonding [1]. Among the *s–p* intermetallics, we can identify three important classes, viz. Hume-Rothery phases, polar intermetallics and Zintl phases that provide a rich collection of structures and electronic properties to study the subtle variations among metals, salts and covalently bonded solids. Intermetallic Zintl phases form between electropositive active metals and electronegative metals, e.g., NaTl, to give valence compounds that are typically semi-conducting (or even semi-metallic) and have narrow homogeneity widths (“line compounds”) [2,3]. Hume-Rothery phases involve combinations of late transition metals with post-transition elements including Al whose structures vary with valence electron concentration but form over wide phase widths [4]. Polar intermetallics represent the class of compounds intermediate between these two because they involve combinations of active metals with late transition metal/post-transition metals in definite compositions but over a range of valence electron concentrations [5].

Synthetic efforts on *AE*–Zn–Al systems (*AE* = Mg, Ca, Sr, Ba) have identified several polar intermetallic compounds, e.g., $BaZn_{10}Al_2$ [6] (vec = 2.33; vec = valence electron concentration = number of valence electrons/number of electronegative atoms (i.e., Zn + Al) in the formula unit), $(Mg_xLi_{1-x})_{2-z}(Zn_yAl_{1-y})_{3+z}$ [7,8] (vec = 2.0–2.4) and $AeZn_xAl_{4-x}$ (*Ae* = Ca, Sr, Ba; $x=0-2$; vec = 3.0–3.5) [9]. These compounds show different Zn/Al networks with vec ranges between 2.0 and 3.25. Like Hume-Rothery phases, compounds with phase widths were observed in $(Mg_xLi_{1-x})_{2-z}(Zn_yAl_{1-y})_{3+z}$ and $AeZn_xAl_{4-x}$ systems. On the other hand, $BaZn_{10}Al_2$ (vec = 2.33) shows a fixed composition, similar to Zintl phases. Theoretical calculations of the electronic structures of these compounds indicate that the bonding characteristics of the Zn–Al framework have an important influence on the phase width and chemical composition of these systems. For example, the observed phase width in the crystalline approximants to

*Corresponding author. Fax: +1-515-2940105.
*E-mail address:* gmiller@iastate.edu (G.J. Miller).

0022-4596/03/$ - see front matter © 2002 Elsevier Science (USA). All rights reserved.
PII: S0022-4596(02)00032-4

quasicrystals, $(Mg_xLi_{1-x})_{2-z}(Zn_yAl_{1-y})_{3+z}$ can be understood by a range of nonbonding orbitals associated with the [Zn,Al] framework for the valence electron concentration between 2.00 and 2.25 electrons/atom [7,8]. No such nonbonding regions are seen in the densities of states (DOS) of the $NaZn_{13}$-type compounds [10]. Furthermore, the atomic site preferences for Zn and Al atoms in these various structures are affected by the coordination environment and the size of alkaline earth metals [11].

During investigations of the $Ba(Zn_xAl_{1-x})_2$ system ($x = 0.0-1.0$; vec = 3.0–4.0), a new ternary compound, $Ba_{14}Zn_{5-x}Al_{22+x}$, was discovered that contains an unprecedented layer of Zn and Al atoms. The structure is intermediate between the cubic Laves phase $BaAl_2$ and $Ba_7Al_{13}$. In this paper, we report the structural characterization, electronic structure and chemical bonding of this new intermetallic compound.

## 2. Experimental

### 2.1. Synthesis and characterization

All reactions were carried out in an Ar-filled glovebox with the concentration of $O_2$ lower than 10 ppm. Starting materials included Ba turnings (Johnson-Matthey, 99.9%), Zn powder (Alfa, 99.9%), Al ingot (Alfa, 99.9999%), and Al foil. The exploratory reactions of $Ba(Zn_xAl_{1-x})_2$ with $x$ varying from 0.0 to 1.0 were performed in sealed Ta ampoules placed in a fused silica Schlenk tube. Reactant mixtures were heated to 900°C under dynamic vacuum for 6 h, then cooled to 400°C at the rate of 5°C/h, and finally rapidly cooled to room temperature. Each product appears as brittle, silvery ingots that are both air and moisture sensitive. The surfaces of all products turned from silver to dark black in 2 days inside the glovebox.

Preliminary characterization of products from these reactions using Guinier powder X-ray diffraction (Enraf-Nonius Guinier camera, Cu$K\alpha_1$ radiation ($\lambda = 1.54056$ Å), internal standard = Si powder) always showed mixtures. Products from Zn-rich reactions, $x \geqslant 0.4$, gave various mixtures of known binary phases ($BaZn_2$, $BaZn_5$, $BaAl_4$ and $Ba_7Al_{13}$). On the other hand, interesting results were observed for products from the Al-rich region. Powder X-ray diffraction patterns from products of two of these reactions ($Ba(Zn_xAl_{1-x})_2$: $x = 0.2$ and 0.25; both quenched as well as slowly cooled) very closely resembled the calculated pattern of $Ba_7Al_{13}$, except for a weak diffraction maximum at $2\theta \sim 10°$. Preliminary single-crystal X-ray diffraction experiments suggested a composition near $Ba_7Zn_3Al_{10}$.

Subsequent reactions targeting $Ba_7(Zn_xAl_{1-x})_{13}$ ($x = 0.23$, 0.38 and 0.62) using the same heating and cooling procedures produced the new phase only for $x = 0.23$. Single-crystal X-ray diffraction was carried out on several crystals isolated from this product and gave the approximate formula, $Ba_{14}Zn_5Al_{22}$. Further reactions based on this final composition gave nearly pure phase of the title compound with trace amounts of Al.

### 2.2. Single-crystal X-ray analysis and structure determination

Needle- and plate-shaped crystals were selected from crushed products in an Ar-filled glovebox, mounted and sealed inside a glass capillary, and checked by means of rotation photographs on Siemens P4 or Rigaku AFC6R diffractometers or by Laue photographs. Most of these crystals gave either a hexagonal unit cell that was close to the unit cell of $Ba_7Al_{13}$ or a $\sqrt{3}a \times b \times c$ supercell, but subsequent refinements indicated unreasonable interatomic distances and temperature displacement factors. In fact, though many of the samples were twinned crystals, a small, needle-shaped crystal ($0.05 \times 0.08 \times 0.3\,mm^3$) extracted from the product with target composition "$Ba_7Zn_3Al_{10}$" were used for single-crystal data collection on a Siemens SMART1000 CCD single-crystal diffractometer (Mo$K\alpha$ radiation, $\lambda = 0.71073$ Å). The intensity data were collected from the whole sphere of reciprocal space at 298(2) K for $2\theta$ values between 3° and 58°. The data were corrected for Lorentz and polarization effects. Also, absorption corrections were based on fitting a function to the empirical transmission surface as sampled by multiple equivalent reflections. Least-squares refinement of the intensity data gave a monoclinic (nearly orthorhombic) unit cell that is close to a $\sqrt{3}a \times b \times 2c$ supercell of the hexagonal unit cell of $Ba_7Al_{13}$ ($a_0 = 6.099(2)$ Å, $c_0 = 17.269(6)$ Å): $a = 10.474(2)$ Å, $b = 6.0834(14)$ Å, $c = 34.697(8)$ Å, and $\beta = 90.814(4)°$. Since the $\beta$ angle is very close to 90°, zone photos of ($0kl$), ($h0l$) and ($hk0$) planes were taken to check their reflection symmetry and confirmed the monoclinic unit cell. A Wilson test indicated a centrosymmetric structure, so the space group was assigned as $I2/m$ (to compare with the $Ba_7Al_{13}$-type structure, we have utilized the unconventional space group). The structure was solved by direct methods and refined by full-matrix least-squares refinement of $F_0^2$ using the SHELXTL 5.12 package [12]. The Ba sites were 100% occupied and four of the 11 "Al sites" showed mixed occupation by Zn and Al atoms to give a final refined composition of $Ba_{14}Zn_{4.76(5)}Al_{22.24}$. The final structural refinement with anisotropic thermal displacement parameters on each site gave $R$-factors of $R_1/wR_2 = 0.0585/0.1651$ for all data and the highest residual electron density is $4.196\,e^-/Å^3$ (0.80 Å from Ba2). Important crystallographic data, positional, site occupation and thermal displacement parameters, and

selected interatomic distances for $Ba_{14}Zn_{5-x}Al_{22+x}$ are listed in Tables 1–3.

The calculated X-ray powder diffraction pattern for $Ba_{14}Zn_{5-x}Al_{22+x}$ closely resembles the calculated pattern of $Ba_7Al_{13}$ in the $2\theta$ range between $10^\circ$ and $50^\circ$, which can make its identification by X-ray powder diffraction difficult. However, there are two reflections, (002) and (004), on the calculated pattern of $Ba_{14}Zn_{5-x}Al_{22+x}$ at low angle ($2\theta \leqslant 10^\circ$) that do not occur in the pattern for $Ba_7Al_{13}$. The Guinier X-ray powder patterns for our $Ba_{14}Zn_{5-x}Al_{22+x}$ samples only found the (004) line near $2\theta = 10^\circ$.

Before discussing the structure and chemical bonding in $Ba_{14}Zn_{5-x}Al_{22+x}$, we should mention that before the structure solution and refinement of the X-ray diffraction data, about 4% of all reflections could not be indexed. These reflections are located at $2\theta$ values exceeding $30^\circ$, and can be assigned to a minor contribution of a twin component. The orientation matrix between the refined model and the twin component is

$$\begin{pmatrix} a' \\ b' \\ c' \end{pmatrix} = \begin{pmatrix} 1-2\sin(90^\circ-\beta) & 0 & 0 \\ 0 & 1 & 0 \\ 0 & 0 & -1 \end{pmatrix} \begin{pmatrix} a \\ b \\ c \end{pmatrix},$$

$\beta = 90.8^\circ$.

The diffraction maxima between the main crystal and twinned crystal are very close because the $\beta$ angle is near $90^\circ$. According to the image data, overlapping diffraction peaks do not split until $2\theta$ is larger than $30^\circ$. The remaining poorly fit reflections ($\sim 6\%$ of all reflections) show narrow peak widths along the $a^*$ and $b^*$ axes ($\Delta\theta < 0.8^\circ$) and wide peak widths along the $c^*$-axis

Table 1
Crystal data and conditions of data collection for $Ba_{14}Zn_{4.76(5)}Al_{22.24}$

| Refined composition | $Ba_{14}Zn_{4.76(5)}Al_{22.24}$ |
|---|---|
| Instrument; Temperature (K) | Smart CCD; 298(2) |
| Formula weight (g/mol) | 5676.36 |
| Crystal size ($mm^3$) | $0.05 \times 0.08 \times 0.3$ |
| Space group, $Z$ | $I2/m$ (No. 14), 2 |
| $a$ (Å) | 10.474(2) |
| $b$ (Å) | 6.0834(14) |
| $c$ (Å) | 34.697(8) |
| $\beta$(°) | 90.814(4) |
| $V$ (Å$^3$) | 2210.5(9) |
| $d_{calc}$ (g/cm$^3$) | 4.264 |
| $2\theta_{max}$ | 57.76° |
| $\mu$ ($mm^{-1}$) | 15.264 |
| Transmission range | 0.455–1.000 |
| Number of reflections collected | 13178 |
| Number of independent reflections | 2952 [$R_{int} = 0.0812$] |
| Data/restraints/parameters | 2952/4/126 |
| Extinction coefficient | 0.00004(4) |
| $R_1$, w$R_2$ (all data)[a] | 0.0585, 0.1651 |
| $R_1$, w$R_2$ ($I > 2\sigma(I)$) | 0.0524, 0.1546 |
| Goodness-of-fit on $F^2$ | 1.099 |
| ($\Delta\rho$) max, min (e$^-$/Å$^3$) | 4.196, −2.323 |

[a] $R_1 = \sum|F_o - F_c| / \sum|F_o|$; $wR_2 = \left[\sum[w(F_o^2 - F_c^2)^2] \sum[w(F_o^2)^2]\right]^{1/2}$, $w = \sigma_F^{-2}$.

Table 2
Atomic coordinates, site occupancies and isotropic displacement parameters (Å$^2$) for $Ba_{14}Zn_{4.76(5)}Al_{22.24}$

| Atom | Site | $x$ | $y$ | $z$ | $U_{eq}$ | Site occ. |
|---|---|---|---|---|---|---|
| Ba1 | 4*i* | 0.5032(1) | 0 | 0.0535(1) | 0.016(1) | |
| Ba2 | 4*i* | 0.9748(1) | $\frac{1}{2}$ | 0.0544(1) | 0.018(1) | |
| Ba3 | 4*i* | 0.8253(1) | 0 | 0.0898(1) | 0.013(1) | |
| Ba4 | 4*i* | 0.8337(1) | 0 | 0.1966(1). | 0.013(1) | |
| Ba5 | 4*i* | 0.3296(1) | $\frac{1}{2}$ | 0.1971(1) | 0.013(1) | |
| Ba6 | 4*i* | 0.3294(1) | $\frac{1}{2}$ | 0.0882(1) | 0.013(1) | |
| Ba7 | 4*i* | 0.5026(1) | 0 | 0.2486(1) | 0.024(1) | |
| *M*8 | 8*j* | 0.2223(2) | 0.2074(4) | 0.0087(1) | 0.022(1) | Zn 0.842(4) Al 0.158 |
| *M*9 | 2*a* | 0 | 0 | 0 | 0.018(2) | Zn 0.191(4) Al 0.809 |
| *M*10 | 4*i* | 0.6184(4) | $\frac{1}{2}$ | 0.0144(1) | 0.023(1) | Zn 0.386(4) Al 0.614 |
| *M*11 | 4*i* | 0.6573(5) | $\frac{1}{2}$ | 0.0895(1) | 0.014(1) | Zn 0.214(4) Al 0.786 |
| Al12 | 4*i* | 0.11648(6) | 0 | 0.2018(2) | 0.014(1) | |
| Al13 | 4*i* | 0.8346(7) | 0 | 0.2975(2) | 0.014(2) | |
| Al14 | 8*j* | 0.5720(4) | 0.2311(8) | 0.1458(1) | 0.015(1) | |
| Al15 | 8*j* | 0.10778(4) | 0.2604(8) | 0.1430(1) | 0.015(1) | |
| Al16 | 4*i* | 0.1616(6) | 0 | 0.811(2) | 0.013(1) | |
| Al17 | 4*i* | 0.3360(6) | 0 | 0.1434(2) | 0.015(2) | |
| Al18 | 4*i* | 0.8428(6) | $\frac{1}{2}$ | 0.1454(2) | 0.015(2) | |

$U_{eq}$ is defined as one-third of the trace of the orthogonalized $U_{ij}$ tensor.

Table 3
Interatomic distances (Å) less than 3.00 Å for $Ba_{14}Zn_{4.76(5)}Al_{22.24}$

| Contacts | Distance (Å) | Contacts | Distance (Å) |
|---|---|---|---|
| *M*8–*M*8 | 2.524(5) | Al13–Al14 | 2.729(7) |
| *M*8–*M*9 | 2.662(2) | Al13–Al18 | 2.736(9) |
| *M*8–*M*11 | 2.575(4) | | |
| *M*8–Al16 | 2.889(6) | Al14–Al14 | 2.811(10) |
| | | Al14–Al17 | 2.844(7) |
| *M*10–*M*10 | 2.661(9) | | |
| *M*10–*M*11 | 2.633(7) | Al15–Al15 | 2.915(10) |
| | | Al15–Al16 | 2.819(7) |
| *M*11–Al14 × 2 | 2.708(6) | Al15–Al18 | 2.863(7) |
| *M*11–Al18 | 2.724(8) | | |
| | | Al16–Al17 | 2.812(9) |
| Al12–Al15 | 2.728(7) | | |
| Al12–Al17 | 2.724(9) | | |

($\Delta\theta > 0.8^\circ$). Therefore, a superstructure with large unit cell constants along the *c*-axis may exist. We contend that these overlapping diffraction peaks from twinning create the large *R*-values in our refinement.

### 2.3. Electronic structure calculations

Tight-binding linear muffin–tin orbital (TB-LMTO-ASA) electronic band structure calculations were carried out on $Ba_{14}Zn_{5-x}Al_{22+x}$ ($x = 1$; i.e., $Ba_{14}Zn_4Al_{23}$), $BaZn_2$, $BaAl_2$ and $Ba_7Al_{13}$ in the atomic sphere approximation using the LMTO47 program [13]. The $x = 1$ model for $Ba_{14}Zn_{5-x}Al_{22+x}$ was utilized to reflect the observed site occupancies (four crystallographic sites have mixed Zn/Al occupancy, but only the site *M*8 showed mostly Zn atom occupation). Exchange and correlation were treated within the local density approximation. All relativistic effects except spin–orbit coupling were taken into account using a scalar relativistic approximation. The radii of the Wigner–Seitz (WS) spheres were obtained by requiring the overlapping potential to be the best possible approximation to the full potential according to an automatic procedure that limited sphere overlap to 19%—at this setting, no empty spheres were necessary [14]. (Note: if the default criterion of 16% sphere overlap is maintained, then 106 empty spheres with WS radii ranging from 0.573–1.128 Å distributed among 31 distinct sites were necessary, but it then became impossible to carry out certain analyses of the electronic structure due to the size of problem.) The WS radii determined by this procedure for the atoms in "$Ba_{14}Zn_4Al_{23}$", $BaAl_2$ and $Ba_7Al_{13}$ are 1.999–2.504 Å for Ba, 1.503–1.590 Å for Zn and 1.547–1.731 Å for Al. The basis set included Ba 6*s*, 6*p* and 5*d* orbitals, Zn 4*s*, 4*p* and 3*d* orbitals, Al 3*s*, 3*p* and 3*d* orbitals and *s* and *p* orbitals at the empty spheres. Furthermore, the Al 3*d* and Ba 6*p* orbitals were treated by the Löwdin downfolding technique [13]. The **k**-space integrations to determine the self-consistent charge density, DOS and crystal Hamilton orbital populations (COHP) were performed by the tetrahedron method using 95, 47, 31 and 56 **k**-points, respectively, in the irreducible wedges of the Brillouin zones for $BaZn_2$, $BaAl_2$, $Ba_7Al_{13}$ and $Ba_{14}Zn_4Al_{23}$.

In addition to TB-LMTO-ASA calculations, semi-empirical extended Hückel tight-binding band calculations [15–18] were carried out on a hypothetical formula, $[Al_{27}]^{(28-n)-}$, to study the "coloring problem" [11], i.e., the site preference problem for Zn and Al throughout the anionic network in $Ba_{14}Zn_{5-x}Al_{22+x}$. The valence orbitals of the Ba atoms were excluded from these calculations, but their two valence electrons were utilized and various valence electron counts ranging from $[Al_{27}]^{(28)-}$ ($x = 5$) to $[Al_{27}]^{(23)-}$ ($x = 0$) were examined. Mulliken populations for valence orbital occupations were evaluated by integrating over a special points set of 100 **k**-points in the irreducible wedge of the primitive monoclinic Brillouin zone [19]. Atomic orbital parameters are: $H_{ii}(3s) = -12.3$ eV, $H_{ii}(3p) = -6.5$ eV, $\zeta(3s) = \zeta(3p) = 1.167$.

## 3. Results and discussion

$Ba_{14}Zn_{5-x}Al_{22+x}$ was discovered while attempting to examine the variation in Laves-type intermetallic structures along the series $Ba(Zn_xAl_{1-x})_2$. $BaAl_2$ was prepared at 3 GPa and 1273 K [20], but it appears to be metastable with respect to $Ba_7Al_{13}$ after quenching to standard temperature and pressure. The structure of $BaAl_2$ is the cubic Laves phase structure of $MgCu_2$, which can be described as a three-dimensional (3D) network of vertex-sharing $[Al_4]$ tetrahedra with Ba atoms in the large interstices, i.e., $Ba[Al_{4/2}]$. On the other hand, $BaZn_2$ [21] adopts the orthorhombic $CeCu_2$ structure type, which is related to both the $AlB_2$, as well as the stuffed hexagonal wurtzite structure [22]. In this structure, each Zn atom is four-bonded (nearly tetrahedral) to other Zn atoms with Ba atoms also occupying the large interstitial spaces. Although $BaAl_2$ and $BaZn_2$ have 3D structural features, $Ba_{14}Zn_{5-x}Al_{22+x}$ has two-dimensional (2D) features closer to $Ba_7Al_{13}$ [23]. The additional Ba atoms in $Ba_7Al_{13}$, i.e., "$Ba_{1.077}Al_2$," cause the cubic 3D network of vertex-sharing $[Al_4]$ tetrahedra of $BaAl_2$ to break up into slabs. Indeed, $Ba_7Al_{13}$ shows 2D $[Al_{13}]$ slabs, but there are $[Al_4]$ tetrahedra sharing a common face to give layers of $[Al_5]$ trigonal bipyramids (tbps) sandwiching a kagomé net of Al atoms (note: the structure of $Ba_7Al_{13}$ may need to be reinvestigated because the Al atom on the kagomé network gave an unreasonable isotropic thermal parameter [23]). The layer of tbps is observable in the hexagonal $MgZn_2$-type Laves phase [22], while

the arrangement of Al atoms in $Ba_7Al_{13}$ resembles slabs cut out of the $MgNi_2$-type Laves phase ($MgNi_2$ shows features of both $MgZn_2$ and $MgCu_2$: there are layers of tbps as well vertex-sharing tetrahedra [22]). See Fig. 1 for illustrations of these three structure types.

### 3.1. Structure description

The complete view of $Ba_{14}Zn_{5-x}Al_{22+x}$ (99% probability thermal ellipsoids) along the [100] direction is shown in Fig. 2. The structure contains discrete 2D $[Zn_{5-x}Al_{22+x}]$ slabs, shown in Fig. 3, with Ba atoms in

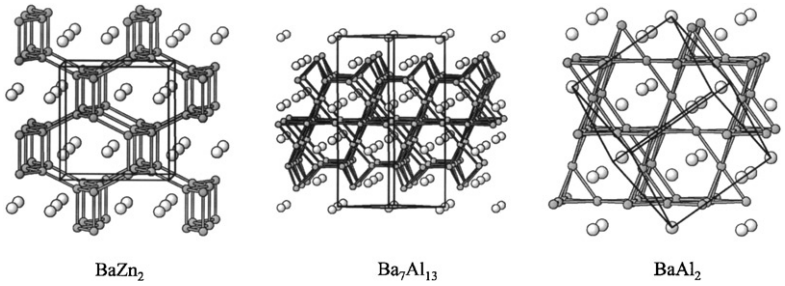


Fig. 1. Views of structures related to $Ba_{14}Zn_{5-x}Al_{22+x}$: $BaZn_2$, $Ba_7Al_{13}$ and $BaAl_2$. Ba: large white circles; Al: small light gray circles; Zn: small dark gray circles. Dark gray sticks indicate distances less than 3.00 Å between pairs of electronegative metal atoms. The unit cell is also shown.

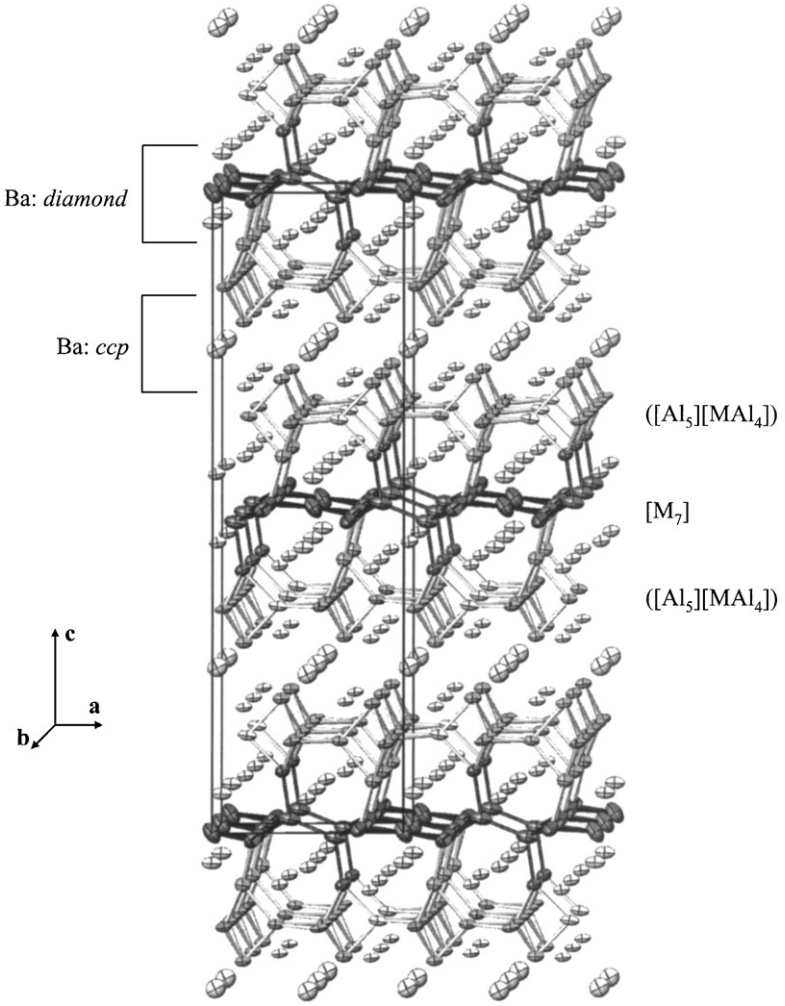


Fig. 2. A perspective view of the structure of $Ba_{14}Zn_{5-x}Al_{22+x}$ along the [010] direction using 99% probability thermal ellipsoids to represent the elements. Ba: white ellipsoids; Al: light gray ellipsoids; Zn: dark gray ellipsoids. Lines indicate distances less than 3.00 Å between pairs of electronegative metal atoms. The unit cell is also shown.

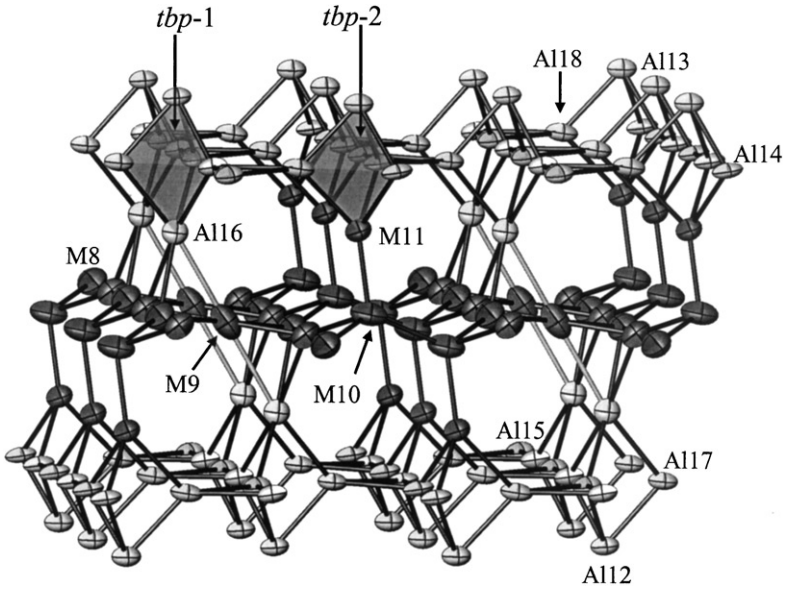


Fig. 3. A single $[Zn_{5-x}Al_{22+x}]$ slab in $Ba_{14}Zn_{5-x}Al_{22+x}$ that identifies the different crystallographic sites for $M$ (Zn/Al mixed sites) and Al atoms. Distances less than 3.00 Å are indicated and the two different types of tbps are labeled.

the interstitial regions. The $[Zn_{5-x}Al_{22+x}]$ slab is similar to the Al substructure of $Ba_7Al_{13}$ and can be described according to the structural formula, $^2_\infty\{([Al_5][MAl_4])\text{-}[M_7]\text{-}([Al_5][MAl_4])\}$, $M = Zn + Al$. As both Fig. 3 and the structural formula indicate, Zn atoms are found only on atomic positions in the central region of the slab, and all Zn/Al mixed occupied sites are four bonded ($d(M-M) < 3.00$ Å). Both $Ba_7Al_{13}$ and $Ba_{14}Zn_{5-x}Al_{22+x}$ contain layers of tbps of the electronegative metals sandwiching another metal layer, but differ in the structures of these intermediate layers: $Ba_{14}Zn_{5-x}Al_{22+x}$ shows a novel 2D $[M_7]$ layer that we will describe shortly. Each layer of tbps in $Ba_{14}Zn_{5-x}Al_{22+x}$ involves two different clusters: $[Al_5]$ (tbp-1) and $[MAl_4]$ (tbp-2) units, where $M$ is approximately 21% Zn (see the shaded clusters in Fig. 3). The average interatomic distance between two tbp units is 2.86 Å, which is shorter than the average intra-atomic distances within each tbp cluster of 3.06 Å. The results of electronic structure calculations on the $^2_\infty[Al_5]$ layer in, e.g., $Ba_3Al_5$ and $Ba_4Al_5$ indicate that the interaction between two tbp clusters is stronger than intracluster bonding along the equatorial edges of the tpb clusters [3], which is also consistent with results we obtain for $Ba_{14}Zn_{5-x}Al_{22+x}$ (see the next section). Consequently, the intercluster distances are typically shorter than the intracluster distances. The observed distances in $Ba_{14}Zn_{5-x}Al_{22+x}$ are consistent with the structural data of $Ba_7Al_{13}$ [23], $Ba_3Al_5$ [24] and $Ba_4Al_5$ [25].

The primary novel aspect of $Ba_{14}Zn_{5-x}Al_{22+x}$ is the 2D $[M_7]$ network at the center of the Zn–Al slab. The refined formula for this net, based upon X-ray diffraction, is close to $[Zn_{4.3}Al_{2.7}]$ with each site of the occupied

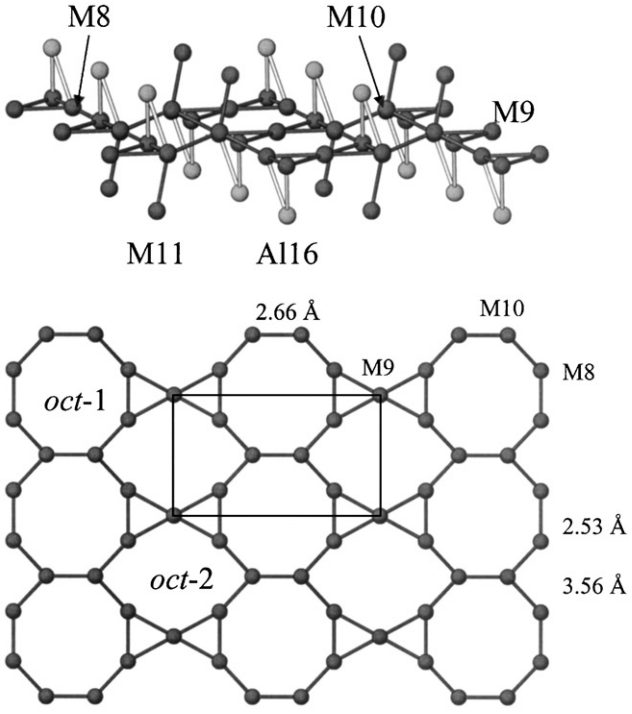


Fig. 4. Two views of the $[M_7]$ layer in $Ba_{14}Zn_{5-x}Al_{22+x}$. (Top) A perspective view along the [010] direction illustrating the connectivity of the atoms to other electronegative metals. (Bottom) A view along [001] emphasizing the ring structure.

by nonrandom mixtures of Zn and Al atoms. The site richest in Zn ($M8$) forms alternating short–long contacts along the $b$-axis, and its coordination environment is close to tetrahedral (see Figs. 3 and 4). The site at the

unit cell origin ($M9$) is mostly Al and is connected to four $M8$ atoms lying nearly in the (001) plane and two Al16 atoms above and below this plane to form two corner-sharing tetrahedra. The local structure around each $M9$ atom closely resembles the environment surrounding Al atoms in the kagomé net of $Ba_7Al_{13}$ or $BaAl_2$. The final site of the 2D [$M_7$] network ($M10$) generates $M10$–$M10$ pairs parallel to the $a$-axis. Each $M10$–$M10$ pair is coordinated to four $M8$ and two $M11$ atoms to form a fragment similar to the staggered ethane structure (see Fig. 4). This local geometry around the $M10$–$M10$ pair is similar to the coordination environment of a Zn−Zn pair in the structure of $BaZn_2$ (see Fig. 1 for the structure of $BaZn_2$). Therefore, the local structure in the central region of the $[Zn_{5-x}Al_{22+x}]$ slab contains aspects of the partial structures of $Ba_7Al_{13}$ and $BaZn_2$, while the outer region corresponds to that of $Ba_7Al_{13}$.

Another way to describe the structure of the 2D [$M_7$] sheet is based on the polygons making up the net, which involve two types of octagons (oct-1 and oct-2) and triangles, shown in Fig. 4. The oct-1 units consist of two $M8-M8$ pairs and two $M10-M10$ dimers connected along the $b$-axis by sharing $M10-M10$ edges. The oct-2 units involve four $M8$, two $M9$ and two $M10$ atoms linked along the $b$-axis by sharing the $M9$ corners. These two octagons share two $M8$ and one $M10$ atoms to create the layer. The structure of the 2D [$M_7$] layer, therefore, can be written $(3838)(38^3)_4(8^3)_2$ based on the number of triangular faces (3) or octagon rings (8) generated around each individual position ($M8 = 38^2$, $M9 = 3838$, $M10 = 8^3$) [22]. The corresponding kagomé net in $Ba_7Al_{13}$ is written as a (3636) network because all points have identical environments [22].

The Ba atoms (represented by white ellipsoids in Fig. 2) form two types of stacking patterns in $Ba_{14}Zn_{5-x}Al_{22+x}$, labeled in Fig. 2. One arrangement is a distorted cubic close packed (*ccp*) structure (Ba4, Ba5 and Ba7) at the outer regions of the $[Zn_{5-x}Al_{22+x}]$ slab and the second type is a distorted diamond structure (Ba1, Ba2, Ba3 and Ba6) at the interior region of the $[Zn_{5-x}Al_{22+x}]$ slab. These two arrangements give rise to four types of Zn/Al polyhedra surrounding the Ba atoms (Ba···Zn/Al distances $< 4.00$ Å), which are irregularly shaped with 12, 13 (two types) and 14 vertices. Ba atoms cap all distorted hexagonal, heptagonal and octagonal faces of these polyhedra to create the two distinct packing arrangements. The average distance between Ba atoms across these faces is 3.8(1) Å, so there is very little Ba–Ba bonding in this compound. This feature contrasts with the single polyhedral environment around Ba atoms in $Ba_7Al_{13}$: a 12-vertex Friauf polyhedron (a truncated tetrahedron) [23].

In summary, the structure of $Ba_{14}Zn_{5-x}Al_{22+x}$ may be considered as an intermediate structure type between $BaAl_2$ and $Ba_7Al_{13}$. This comparison is illustrated in Fig. 5. The $BaAl_2$- (cubic $MgCu_2$-type Laves phase) and $MgZn_2$-type (hexagonal Laves phase) structures represent two extreme modes of fused Friauf polyhedral networks (Fig. 5a): [22,26] the $MgCu_2$-type contains vertex-sharing tetrahedra and the $MgZn_2$-type contains layers of tbps. Furthermore, for Ba concentrations at 33.3 atomic percent, i.e., $BaM_2$, the electronegative component adopts a 3D structure ($BaAl_2$, $BaZn_2$). When the Ba concentration increases, the networks of the electronegative metals transformed to 2D structures, e.g., $Ba_7Al_{13}$, $Ba_{14}Zn_5Al_{22}$, $Ba_3Al_5$ and $Ba_4Al_5$. The partial structure of $Ba_7Al_{13}$ contains combinations of $MgCu_2$- and $MgZn_2$-type structures (Fig. 5b). On the other hand, similar slabs in $Ba_{14}Zn_{5-x}Al_{22+x}$ preserve the $MgZn_2$-type fragment, but the central region contain fragments similar to both $MgCu_2$ (or $Ba_7Al_{13}$ partial structure) and $BaZn_2$ structure types (Fig. 5b). Finally, only layers of tbp clusters exist in the structures of $Ba_3Al_5$ and $Ba_4Al_5$ (Fig. 5c). That the dimensionality of the Zn/Al network drops as the concentration of Ba increases resembles what happens in Zintl phases: addition of more electropositive metals adds valence electrons to the network of electronegative atoms and causes covalent bonds to break [5,27,28].

### 3.2. Electronic structure and chemical bonding

The DOS and (Zn/Al)–(Zn/Al) –COHP curves obtained from TB-LMTO-ASA calculations on $Ba_{14}Zn_4Al_{23}$ with Zn atoms exclusively in the $M8$ positions (based upon the results of X-ray diffraction; see Table 2) and Al atoms at the remaining mixed occupied sites are shown in Fig. 6. These calculations included the Zn 3*d* orbitals, but since they occur as a narrow band just above −10 eV (bandwidth is ca. 0.7 eV), these orbitals were not included in either the DOS plots or in the COHP analysis. The DOS shows that the occupied states are primarily valence orbitals from the 2D $[Zn_4Al_{23}]$ net, with Ba 6*s* and some 5*d* contributions occurring among the levels within ca. 2 eV below the Fermi level. Furthermore, the DOS at the Fermi level is near a relative minimum value to suggest electronic stability at this composition (indeed, the composition of the calculation is close to the stoichiometry refined from X-ray diffraction data).

The −COHP curves of $M-M$ and Al−Al interactions in the $[Zn_4Al_{23}]$ net further suggest that valence electron concentration is, indeed, influential towards stabilizing this structure against other possibilities: all bonding states in these slabs are filled while antibonding states remain empty. We can also examine the bonding in the 2D $[Zn_4Al_{23}]$ network from the valence electron density. Fig. 7 illustrates contour plots of these densities in the plane (or nearly so!) of the [$M_7$] sheet as well as in the equatorial planes of the sheets of tbps [$(Al_5)_2$]. Some striking observations of these plots indicate: (1) the

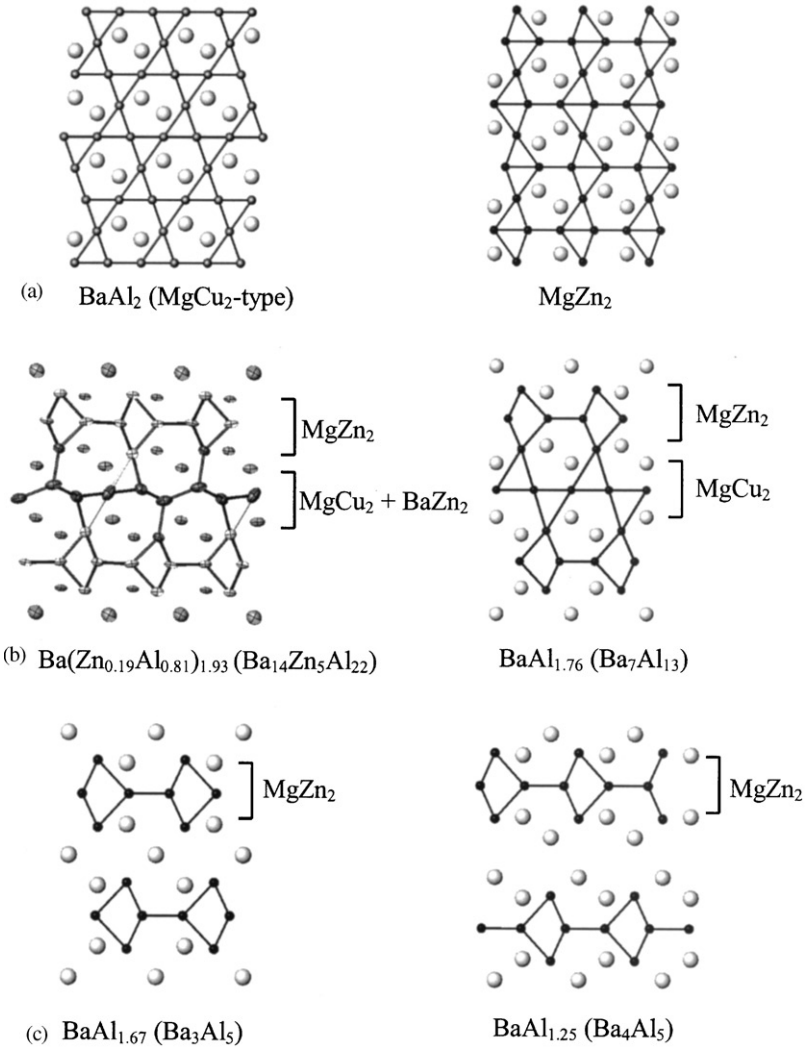


Fig. 5. Projections of various Laves-type structures in the Ba–Zn–Al system. (a) The two limiting Laves phase structures: cubic $MgCu_2$-type observed for $BaAl_2$ and the hexagonal $MgZn_2$–type; (b) $Ba_{14}Zn_{4.76}Al_{22.24}$ and $Ba_7Al_{13}$; and (c) $Ba_3Al_5$ and $Ba_4Al_5$. Large circles are Ba atoms; small dark circles are Al or Zn atoms.

short Zn–Zn distance in the $M_7$ sheet (2.524 Å) does not correlate with a strong covalent bond, but is influenced by their interactions with the Al atoms in the center of the "bow-tie" fragments; (2) all other contacts in the $M_7$ sheet show build-up of electron density as in two-center, two-electron bonds; (3) three-center, two-electron bonds hold the tbps together in the 2D $[(Al_5)_2]$ sheets, but there is some electron density as well within these clusters.

Recent efforts to characterize the chemical bonding and electronic structure in polar intermetallics have identified some important aspects [3,9]: (1) bonding within the network of electronegative metal atoms, according to crystal orbital overlap population (COOP [29]) or crystal orbital Hamilton population (−COHP [30]) curves, is optimized, i.e., bonding states are filled, antibonding states are empty; (2) there is no energy gap separating these states, but the DOS curves often show a minimum value at the Fermi level (a "pseudogap"); and (3) the electropositive metals need not contribute all of their valence electrons to the network of electronegative atoms [3]. Therefore, from points (2) and (3), we can recognize polar intermetallic compounds as distinct from Zintl phases. An example of these points is cubic $BaAl_2$. According to the DOS and −COHP curves in Fig. 8, Al−Al interactions are optimized at the calculated Fermi level, but there is significant contribution from Ba 6*s* and 5*d* orbitals to the occupied states. Earlier theoretical results for $CaAl_2$ suggest the formulation "$Ca^+(Al_2)^-$," which means that Al−Al bonding is optimized for 3.5 valence electrons per Al atom [31]. On the other hand, the analysis for $BaZn_2$ does not follow these guidelines. The $CeCu_2$ structure type for $BaZn_2$ contains a 3D network of Zn atoms that resembles a Zintl-phase. The DOS and −COHP curves demonstrate

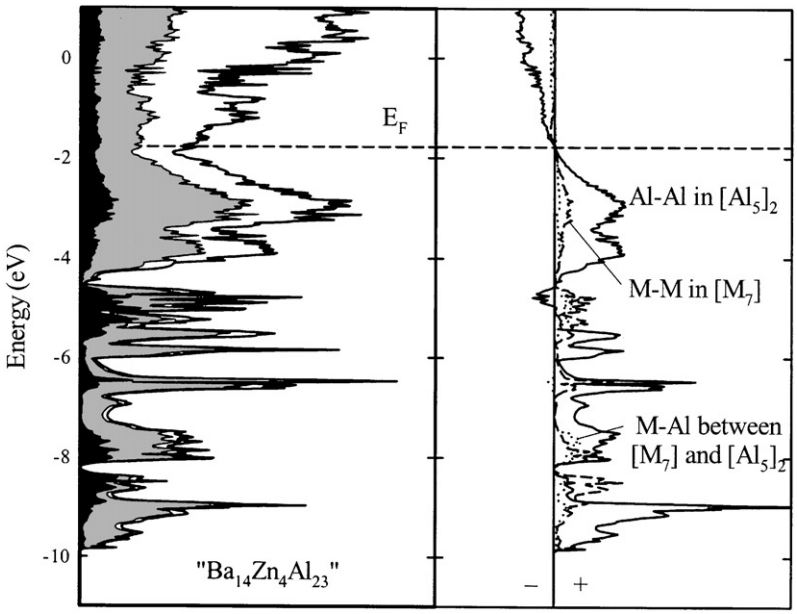


Fig. 6. (Left) Total DOS and partial DOS curves for $Ba_{14}Zn_4Al_{23}$. The shaded region identifies levels from the 2D $[Zn_4Al_{23}]$ slab and the black region shows states from the $[M_7]$ sheet. The Fermi level is labeled. (Right) −COHP curves for three different types of interactions in the 2D $[Zn_4Al_{23}]$ slab: (solid line), Al−Al interactions within the $[Al_5]_2$ slabs; (dashed line), $M-M$ interactions within the $[M_7]$ sheets; and (dotted line), $M$−Al interactions between the $[Al_5]_2$ slabs and the $[M_7]$ sheet.

that Zn−Zn bonding is not optimized at the Fermi level, but that the Fermi level does fall in a deep minimum of the DOS. Earlier theoretical studies of the $CeCu_2$-type structure address issues influencing the distorted tetrahedral coordination at the electronegative elements [32] and have used second moments scaling to identify optimum stability for this "$AB_2$" structure type near seven valence electrons per formula unit [33].

$Ba_{14}Zn_{5-x}Al_{22+x}$ follows the above guidelines for a polar intermetallic compound. So, can we identify an electron counting scheme that accounts for its structure? EHT calculations are useful here because they allow a Mulliken population analysis [34], which provides insight into charge segregation within the framework of electronegative atoms. Table 4 summarizes the Mulliken populations for the different crystallographic sites in the 2D $[Zn_{5-x}Al_{22+x}]$ slab from EHT (i.e., using just Al parameters for all sites). These populations are reported for 105 valence electrons per formula unit: the value at which the (Zn/Al)–(Zn/Al) overlap populations are maximized to be in accord with the −COHP curves for $Ba_{14}Zn_4Al_{23}$ (see Fig. 6). For this valence electron count, we can assign the formal charge of the 2D slab in $Ba_{14}Zn_{4.76}Al_{22.24}$ to be −28.76, which would be closely met by 14 "$Ba^{2+}$" cations in the structure. Among the four crystallographic sites where we find mixed occupancy by Zn and Al atoms, two of these sites have the lowest Mulliken population ($M8$ and $M9$), which makes them good candidates for Zn occupancy relative to Al. On the other hand, although $M9$ has a lower population (3.320) than $M8$ (3.550), $M8$ also has a higher population in the valence $s$ orbital (1.225 vs 1.183). It appears that not only the low total Mulliken population, but also the higher valence $s$ orbital occupation helps to enhance Zn occupation at the $M8$ sites over the $M9$–$M11$ sites.

Surprisingly, the EHT calculations suggest treating Ba as $Ba^{2+}$ in $Ba_{14}Zn_{5-x}Al_{22+x}$, which is inconsistent with its treatment in $BaAl_2$. Even the partial DOS calculated by TB-LMTO-ASA show very little contributions from Ba $6s$ and $5d$ orbitals within the occupied states. To probe these differing aspects of valence charge transfer, we carried out TB-LMTO-ASA and EHT calculations on $Ba_7Al_{13}$ and $Ba_3Al_5$ to study the Al−Al COHP/COOP values. Their DOS and −COHP curves are illustrated in Fig. 9. For each, bonding within the Al atom networks is optimized (or very nearly so in the case of $Ba_3Al_5$!), while EHT analysis of these frameworks finds optimal bonding near 46 and 22 valence electrons per formula unit, respectively, for $Ba_7Al_{13}$ and $Ba_3Al_5$ (i.e., 3.54 and 4.4 valence electrons per Al atom, respectively). Therefore, we can write the following approximate formulations: "$(Ba^+)_7[(Al_{13})^{7-}]$" and "$(Ba^{2+})_3(Al_5)^{6-}$", which suggests that Ba atoms donate more valence electrons to Al atoms as the concentration of Ba increases beyond ca. 35 at% with respect to Al atoms. In $BaAl_2$, there is 33.3 at% Ba, while in $Ba_{14}Zn_{4.76}Al_{22.24}$, there is 34.1 at% Ba with respect to all elements, but 38.6 at% with respect to just Ba and Al atoms. It appears that the Zn atoms provide a reservoir

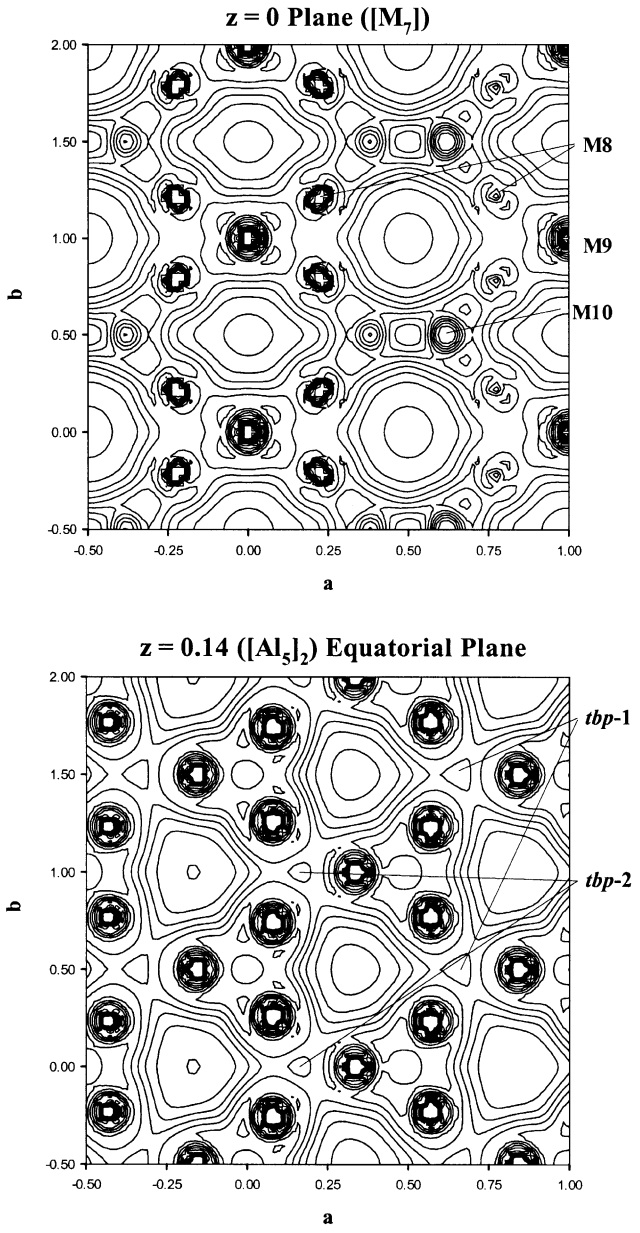


Fig. 7. Contour diagrams of the total valence electron density in the $z = 0$ and 0.14 sheets of $Ba_{14}Zn_4Al_{23}$. Contours are plotted in step sizes of $0.005e^-$ from 0 to $0.05e^-$. The labels along the coordinate axes correspond to fractional coordinates.

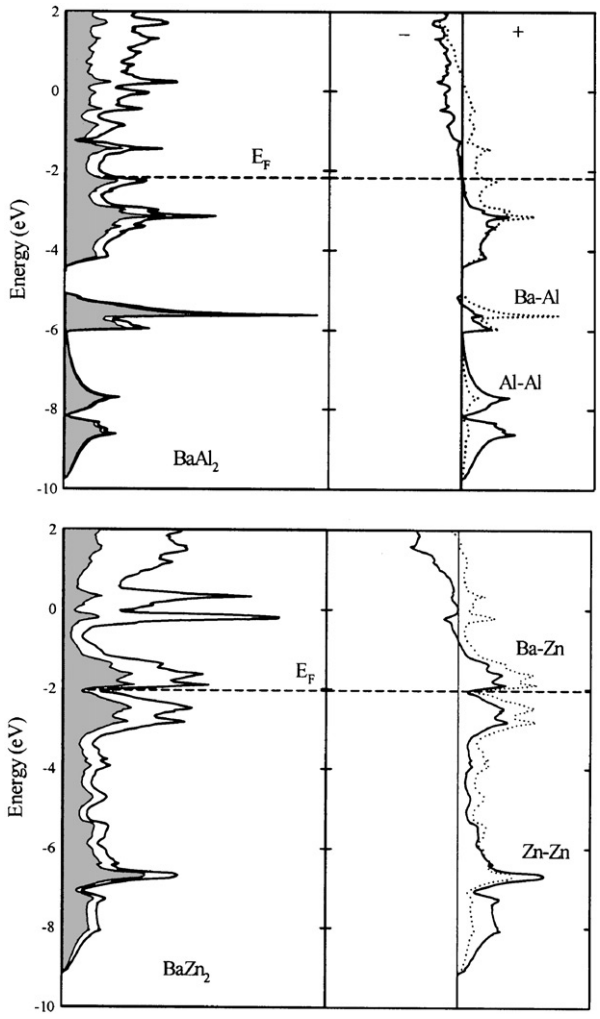


Fig. 8. Total DOS, partial DOS from the electronegative component and −COHP curves for $BaAl_2$ (top) and $BaZn_2$ (bottom). The Fermi levels are indicated.

of ca. two valence electrons in valence 4*s* orbitals, but valence charge transfer is influenced by the concentration of Al atoms.

We conclude this section by proposing an electron counting scheme for these Laves-type, polar intermetallics using the theoretical results. This scheme focuses on $Ba_3Al_5$, $Ba_{14}Zn_{4.76}Al_{22.24}$, $Ba_7Al_{13}$ and $BaAl_2$, and the results of a Mulliken population analysis on the corresponding electronegative metals for each compound at the valence electron count for optimum bonding are listed in Table 4. The results in the table are separated into the various structural building blocks: the first three compounds contain sheets of tbps, while $Ba_{14}Zn_{4.76}Al_{22.24}$ and $Ba_7Al_{13}$ also contain, respectively, $(3838)(3\,8^3)_4(8^3)_2$ and (3636) nets. Note that the number of valence electrons assigned to the tbps increases from ca. 18/tbp in $Ba_7Al_{13}$ to ca. 20/tbp in $Ba_{14}Zn_{4.76}Al_{22.24}$ and then to 21/tbp in $Ba_3Al_5$. In all cases, the valence electron density is higher at the axial positions than in the equatorial plane, where these atoms are also involved in three-center bonding to other tbps (see Fig. 7). The different valence electron counts reflect the various ways these clusters interact with neighboring electronegative metals. In $Ba_3Al_5$, the slabs of tbps are essentially isolated from one another by Ba atoms (see **1**), which means that 20–22 valence electrons per tbp is optimal (we arrive at this range by assigning 5 valence electrons at the apical sites—these are three-bonded—and 3.33–4 valence electrons at the equatorial

Table 4
Mulliken population (MP) analyses of various Ba–Zn–Al structures evaluated at the valence electron count for optimum (Zn/Al)–(Zn/Al) bonding

| $Ba_{14}Zn_{4.76}Al_{22.24}$ | | | $Ba_7Al_{13}$ | | |
|---|---|---|---|---|---|
| Site | Type | MP | Site | Type | MP |
| Al12 | tbp-1-apex (terminal) | $4.98e^-$ | Al1 | tbp-apex (terminal) | $4.46e^-$ |
| Al16 | tbp-1-apex (connected) | $3.83e^-$ | Al2 | tbp-apex (connected) | $3.47e^-$ |
| Al15 (2×) | tbp-1-equat. | $3.64e^-$ | Al3 | tbp-equat. | $3.38e^-$ |
| Al17 | tbp-1-equat. (tbp-1) | $3.74e^-$ ($19.83e^-$) | Al4 | kagomé net | $3.34e^-$ |
| Al13 | tbp-2-apex (terminal) | $4.95e^-$ | $Ba_3Al_5$ | | |
| *M*11 | tbp-2-apex (connected) | $3.97e^-$ | Al1 | tbp-apex (terminal) | $4.90e^-$ |
| Al14 (2×) | tbp-2-equat. | $3.76e^-$ | Al2 | *tbp*-equat. | $3.73e^-$ |
| Al18 | tbp-2-equat. (tbp-2) | $3.74e^-$ ($20.18e^-$) | $BaAl_2$ | | |
| *M*8 (4×) | [$M_7$] | $3.55e^-$ | Al | Kagomé net | $3.50e^-$ |
| *M*9 | [$M_7$] | $3.32e^-$ | | | |
| *M*10 (2×) | [$M_7$] | $3.72e^-$ | | | |
| | [$M_7$] sheet | ($24.96e^-$) | | | |

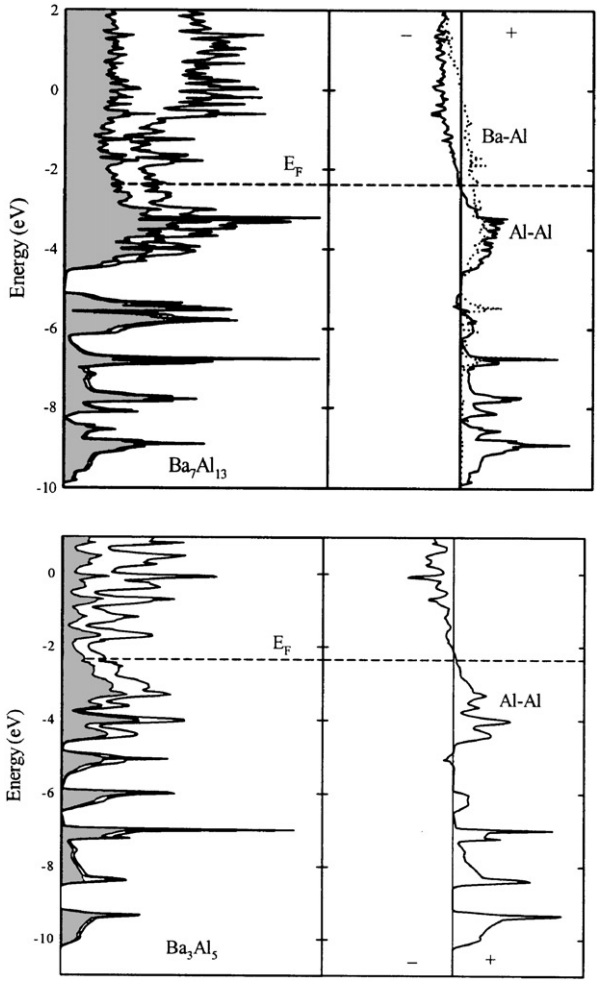


Fig. 9. Total DOS, partial DOS from the electronegative component and −COHP curves for $BaAl_2$ (top) and $BaZn_2$ (bottom). The Fermi levels are indicated.

sites—these are four-bonded, but are also part of the equatorial interactions within the tbp; in the three examples, equatorial distances between tbp are ca. 2.85 Å, whereas within tbp they are ca. 3.22 Å). As these tbps interact with other metal fragments, their average valence electron density drops with the greatest specific decrease occurring at the apical atom of contact, as seen in **2** and **3** for the tbp in $Ba_{14}Zn_{4.76}Al_{22.24}$ and $Ba_7Al_{13}$.

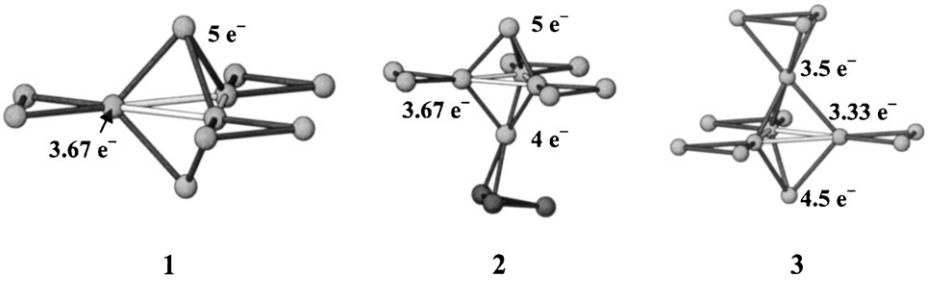


**1** **2** **3**

What remains are the two different nearly planar nets. The $(3838)(38^3)_4(8^3)_2$ [$M_7$] net in $Ba_{14}Zn_{4.76}Al_{22.24}$ is assigned 25 valence electrons (3.57 electrons per atom) while the kagomé (3636) net in $Ba_7Al_{13}$ gets ca. 10 valence electrons (3.33 electrons per atom). These different valence electron concentrations are consistent with the fraction of triangles (3-rings) in each net according to second moments scaling ideas of Burdett and Lee: as the valence electron concentration approaches the half-filled band condition (4 electrons per atom), we expect a decrease in the number of triangles in the network [35].

## 4. Summary

The structure of a new polar intermetallic compound, $Ba_{14}Zn_{5-x}Al_{22+x}$, was determined in this study, which contains a new 2D sheet of atoms containing 8-membered rings. Theoretical calculations on the bonding characteristics within the Zn–Al framework show a sharp transition from bonding to antibonding states at the Fermi level, and suggest that Ba behaves as a two-electron donor, unlike in $BaAl_2$ or $Ba_7Al_{13}$. There seems to be a relationship between valence electron transfer from the active metal to the electronegative components and the composition, which we are continuing to examine in a variety of novel and existing polar intermetallic systems.

## Acknowledgment

This work was supported by the National Science Foundation through NSF DMR 99-81766.

## References

[1] J.H. Westbrook, R.L. Fleischer (Eds.), Intermetallic Compounds: Principles and Practice, Wiley, New York, 1995.
[2] R. Nesper, Prog. Solid State Chem. 20 (1990) 1.
[3] G.J. Miller, in: S.M. Kauzlarich (Ed.), Structure and Bonding at the Zintl Border, VCH, New York, 1996, p. 1.
[4] C.S. Barrett, T.B. Massalski, Structure of Metals, 3rd Edition, Pergamon Press, Oxford, 1980.
[5] H. Schäfer, Ann. Rev. Mater. Sci. 15 (1985) 1.
[6] C.-S. Lee, Experimental and theoretical investigations in alkaline earth–zinc–aluminum intermetallic systems, Ph.D. Thesis, Iowa State University, 2000.
[7] C.-S. Lee, G.J. Miller, J. Am. Chem. Soc. 122 (2000) 4937.
[8] C.-S. Lee, G.J. Miller, Inorg. Chem. 40 (2001) 338.
[9] U. Häussermann, U.S. Amerioun, L. Eriksson, C.-S. Lee, G.J. Miller, J. Am. Chem. Soc. 124 (2002) 4371.
[10] K.J. Nordell, G.J. Miller, Inorg. Chem. 38 (1999) 579.
[11] G.J. Miller, Eur. J. Inorg. Chem. (1998) 523.
[12] G.M. Sheldrick, SHELXTL, Structure Determination Programs; Version 5.12 Edition; Siemens Analytical X-ray Instruments Inc., Madison, WI, 1995.
[13] (a) O.K. Andersen, Phys. Rev. B 12 (1975) 3060.
(b) O.K. Andersen, O. Jepsen, Phys. Rev. Lett. 53 (1984) 2571.
(c) O.K. Andersen, O. Jepsen, D. Glötzel, in: F. Bassani, F. Fumi, M.P. Tosi (Eds.), Highlights of Condensed-Matter Theory, North-Holland, New York, 1985.
(d) O.K. Andersen, Phys. Rev. B 34 (1986) 2439.
[14] O. Jepsen, O.K. Andersen, Z. Phys. B 97 (1995) 35.
[15] R. Hoffmann, W.N. Lipscomb, J. Chem. Phys. 36 (1962) 2179, 3489.
[16] R. Hoffmann, J. Chem. Phys 39 (1963) 1397.
[17] J.H. Ammeter, H.-B. Bürgi, J.C. Thibeault, R. Hoffmann, J. Am. Chem. Soc. 100 (1978) 3686.
[18] M.-H. Whangbo, R. Hoffmann, R.B. Woodward, Proc. R. Soc. London Ser. A 366 (1979) 23.
[19] D.J. Chadi, M.L. Cohen, Phys. Rev. B 8 (1973) 5474.
[20] G. Cordier, E. Czech, H. Schäfer, Z. Naturforsch. B: Anorg. Chem. Org. Chem. 39B (1984) 421.
[21] G. Bruzzone, M. Ferretti, F. Merlo, J. Less-Common Met. 114 (1985) 305.
[22] W.B. Pearson, The Crystal Chemistry and Physics of Metals and Alloys, Wiley-Interscience, New York, 1972.
[23] M.L. Fornasini, G. Bruzzone, J. Less-Common Metals 40 (1975) 335.
[24] M.L. Fornasini, Acta Crystallogr. C 44 (1988) 1355.
[25] M.L. Fornasini, Acta Crystallogr. B 31 (1975) 2551.
[26] P. Villars, L.D. Calvert, Pearson's Handbook of Crystallographic Data for Intermetallic Phases, 2nd Edition, ASM International, Metals Park, OH, 1991.
[27] H. Schäfer, B. Eisenmann, W. Mueller, Angew. Chem. 85 (1973) 742.
[28] (a) R. Nesper, Angew. Chem. 103 (1991) 805.
(b) R. Nesper, Angew. Chem. Int. Ed. Engl. 30 (1991) 789.
[29] (a) T. Hughbanks, R. Hoffmann, J. Am. Chem. Soc. 105 (1983) 3528.
(b) S.D. Wijeyesekera, R. Hoffmann, Organometals 3 (1984) 949.
[30] R. Dronskowski, P. Blöchl, J. Phys. Chem. 97 (1993) 8617.
[31] R. Nesper, G.J. Miller, J. Less-Common Met. 197 (1993) 109.
[32] G. Nuspl, K. Polborn, J. Evers, G.A. Landrum, R. Hoffmann, Inorg. Chem. 35 (1996) 6922.
[33] S. Lee, J. Am. Chem. Soc. 113 (1991) 101.
[34] J.K. Burdett, Molecular Shape, Wiley, New York, 1980.
[35] J.K. Burdett, S. Lee, J. Am. Chem. Soc. 107 (1985) 3050, 3063.